Article

Journal of the Brazilian Chemical Society

https://dx.doi.org/10.21577/0103-5053.20230160

J. Braz. Chem. Soc. **2024**, *35*, 4, e-20230160, 1-15

Photoluminescent and Magnetic Properties of Mononuclear Lanthanide-Based Compounds Containing the Zwitterionic Form of 4-Picolinic Acid as a Ligand

Esther S. Areas,[#,a] Bruno P. Rodrigues,[#,a] Ana Carolina C. do Nascimento,[a] Henrique C. Silva Junior,[a] Glaucio B. Ferreira,[a] Fabio S. Miranda,[a] Flávio Garcia,[b] Syed H. Safeer,[b] Stéphane Soriano[c] and Guilherme P. Guedes[*,a]

[a]*Instituto de Química, Universidade Federal Fluminense, 24020-141 Niterói-RJ, Brazil*

[b]*Centro Brasileiro de Pesquisas Físicas, 22290-180 Rio de Janeiro-RJ, Brazil*

[c]*Instituto de Física, Universidade Federal Fluminense, 24210-346 Niterói-RJ, Brazil*

A series of mononuclear lanthanide-based coordination compounds was obtained under mild synthetic conditions and fully characterized. Single-crystal X-ray diffraction reveals six isomorphic compounds of type $[Ln(NO_3)(4picH)_2(H_2O)_4](NO_3)_2$ (Ln^{3+} = Sm (**1**), Eu (**2**), Gd (**3**), Tb (**4**), Dy (**5**), Er (**6**)), in which 4picH is the zwitterionic form of the 4-picolinic acid. Except for compounds **3** and **6**, a study into the emissive properties of the compounds was carried out, revealing a ligand-sensitized lanthanide-characteristic luminescence. Compounds **2** and **4** are candidates for luminescent probes in solution. At the same time, the chromaticity data for **5** revealed a potential white-light emitter with a correlated color temperature (CCT) value of 6570 K. Alternating current (AC) magnetic susceptibility measurements, supported by theoretical calculations, showed a field-induced slow relaxation of the magnetization and a single-ion magnet behavior for compound **5**.

Keywords: white-light emitter, single-ion magnet, structural analyses and structure determination, theoretical and computational chemistry, coordination chemistry

Introduction

The advent of a new technological order demands from the chemical industry the capacity to controllably and sustainably obtain materials that are able not only to address targeted functions, such as the need for photoluminescence or magnetic properties but are rather designed to display multiple features that ensure their application in different fields of science. For this reason, much attention has been devoted to developing new molecule-based materials, given their capacity to be engineered in a controlled fashion from discrete molecules and have their physical properties directed and predicted, giving rise to new materials possessing appealing features such as plasticity or designability.[1,2]

One of the avenues followed toward new molecular materials is based on coordination compounds. From a synthetic point of view, they can carry desired properties from the ligand and/or metal ions so that a plethora of coordination compounds with different nuclearities, architectures and final properties can be afforded by a huge number of combinations between metal ions and ligands. However, fine-tuning the architecture and final properties in a coordination compound is not a simple task, and some behaviors have been merely obtained by serendipity.

Focusing on technological applications, lanthanide-based compounds have been largely explored in the most diverse applications, such as bioimaging and photodynamic therapy, new sensors, magnetic materials, solar energy converters, luminescent probes, and light-emitting devices.[3-8] For instance, since the discovery of the slow relaxation of the magnetization in lanthanide double-decked phthalocyanine compounds in 2003 by Ishikawa and co-workers,[9] terbium(III) and dysprosium(III) compounds have had an important role in the molecular magnetism field, followed by an exponential growth in the number of synthesized compounds in the last two decades. Furthermore, in addition

*e-mail: guilherme_guedes@id.uff.br
[#]These authors contributed equally to this work.
Editor handled this article: Jaísa Fernandes Soares
This manuscript is part of a series of publications in the Journal of the Brazilian Chemical Society by young researchers who work in Brazil or have a solid scientific connection with our country. The JBCS welcomes these young investigators who brighten the future of chemical sciences.

to the magnetic properties, the typical broad emission (ranging from ultraviolet to near-infrared regions) is seen as a driving force for applications of lanthanide-based coordination compounds as promising new materials.[10,11]

The well-known need for lanthanide ions to be sensitized by energy-transfer mechanisms to overcome the forbidden nature of their electronic transitions afforded a large amount of published works on lanthanide-containing coordination compounds focusing on the choice of antenna ligands. Organic molecules such as heterocyclic derivatives and aromatic carboxylic acids are commonly used due to their structure-directing nature and the possibility to modulate the final properties. The 4-picolinic acid, common to both classes of compounds, is of special interest due to not only possessing light-absorbing features and efficient energy-transferring but also presenting three different coordinating sites, one nitrogen atom and two carboxylic oxygen atoms, enabling the coordination of the ligand both to 3d and/or 4f metal ions. While a considerable amount of papers report extended or heterometallic systems containing lanthanide ions and picolinic acid derivatives,[12-16] it is a surprisingly difficult task to encounter discrete lanthanide complexes of such derivatives, being the picolinic moiety found as a co-ligand in reported systems.[17,18] Additionally, to the best of our knowledge, there are no reports on the zwitterionic form of 4-picolinic acid as a sensitizer.

Regarding light-emitting devices, the white-light emitter ones are of great interest in the new materials field, given their ability to modulate the final color by combining a single chromophore. For example, dysprosium(III)-containing compounds were reported as white-light emitters by Yang *et al*.[19] in which the ligand has a key role in both metal ion sensitizing and contributing to the emission, which could be modulated by the excitation wavelength. White-light emission study in molecular compounds aims for applications in electronic displays and light-emitting devices, replacing mercury-based fluorescent materials, giving rise to a higher luminescence efficiency and reducing environmental risks.[20]

Based on the applications of lanthanide compounds, a combination of luminescent and magnetic properties was explored in a series of mononuclear compounds containing the zwitterionic form of the 4-picolinic acid as a ligand.

Experimental

Materials

All reagents and solvents were purchased from commercial sources and used as received. Ln^{3+}-containing compounds were synthesized using the following reagents: $Sm(NO_3)_3.xH_2O$ (min. 99.9%, Sigma-Aldrich, Saint Louis, USA), $Eu(NO_3)_3.5H_2O$ (min. 99.9%, Sigma-Aldrich, Saint Louis, USA), $Gd(NO_3)_3.6H_2O$ (min. 99.99%, Sigma-Aldrich, Saint Louis, USA), $Tb(NO_3)_3.5H_2O$ (min. 99.9%, Sigma-Aldrich, Saint Louis, USA), $Dy(NO_3)_3.xH_2O$ (min. 99.9%, Sigma-Aldrich, Saint Louis, USA), $Er(NO_3)_3.5H_2O$ (min. 99.9%, Sigma-Aldrich, Saint Louis, USA), 4-picolinic acid (min. 99%, Sigma-Aldrich, Saint Louis, USA) and ethanol (min. 99.9%, Sigma-Aldrich, Saint Louis, USA). Solutions for spectroscopic characterizations were prepared using ethanol, methanol (min. 99.9%, Sigma-Aldrich, Saint Louis, USA), and $BaSO_4$ (min. 99%, Sigma-Aldrich, Saint Louis, USA).

Instrumentation

Compounds purity was evaluated through elemental analyses (CHN) performed on a PerkinElmer CHN 2400 (PerkinElmer, Waltham, Massachusetts, USA). Infrared absorption spectra were obtained in attenuated total reflectance (ATR) mode on a Thermo Varian FT-IR iS50 (Thermo Fischer Scientific, Waltham, Massachusetts, USA) in the 4000-500 cm^{-1} and 600-150 cm^{-1} range (4 cm^{-1} of resolution). Electronic absorption spectra were obtained in the solid state on a Cary 5000 UV-Vis-NIR (Agilent Technologies, Santa Clara, California, USA) using barium sulfate as white reference material in the 200-800 nm spectral range, and in solution, on a Varian Cary 50 spectrophotometer (Agilent Technologies, Santa Clara, California, USA) in the 200-800 nm range. Luminescence measurements were performed on an Edinburgh FLS980 Spectrofluorometer (Edinburgh Instruments, Livingston, UK). Solid-state emission spectra were measured using a front-face sample holder with a resolution of 0.5 nm and an excitation wavelength of 280 nm. All spectra were recorded in the 310-800 nm spectral range, while for the erbium derivative the spectra range was extended to the NIR region (900-1500 nm). Excitation spectra were also acquired under identical conditions, selecting the emission wavelength corresponding to the highest intensity emission for each compound. The emission spectra of compounds **1-6** in ethanolic solution (1.0×10^{-3} mol L^{-1}) were obtained at 298 K, with a resolution of 0.5 nm and an excitation wavelength of 280 nm. For measurements at 77 K, the ethanolic solution of each compound was diluted in a frozen glassy solution (4 EtOH:MeOH) to afford a final concentration of 5.0×10^{-5} mol L^{-1}. Judd-Ofelt parameters and radiative rates were calculated using JOES 4.0 software.[21]

The emission lifetime measurements were carried out in a home-built laser table. Quartz cuvettes (10 mm pathlength) containing the solutions of the compounds

were irradiated by selected wavelengths, using the OPO Rainbow from Quantel excited by the third harmonic of an Nd-YAG pulsed laser (Quantel BRILLIANT-B). The emissions were collected at 90 degrees to the excitation on an Oriel Cornerstonet 260 1/4 m monochromator at the selected wavelengths and detected using a Hamamatsu R12829 PMT. The signals were captured using an oscilloscope (LeCroy Wavesurfer 44MXs-B, 400 MHz). Luminescence lifetimes were obtained by a pulsed laser beam, using excitation wavelengths of 472 nm (for **1**), 465 nm (for **2**), 487 nm (for **4**), and 454 nm (for **5**), following the emission of the lowest luminescent level to the ground state. The decay curves (Figures S1-S12, Supplementary Information (SI) section) were derived from the monitored emissions at 598, 613, 545, and 576 nm for **1**, **2**, **4** and **5**, respectively. The curves were fit by an exponential decay function (ExpDec1) using the OriginLab 9.1 software.[22]

Single crystal data for all compounds were collected at room temperature on a Bruker D8 Venture diffractometer (Bruker AXS, Karlsruhe, Germany) with Mo Kα radiation (λ = 0.71073 Å). Data collection, cell refinement, and data reduction were performed by the Bruker Instrument Service V6.2.6, APEX3, and SAINT software, respectively.[23,24] Absorption corrections were performed by the SADABS software,[25] using the equivalent reflections method. The structure solutions and full-matrix least-squares refinements were performed with the SHELXS and SHELXL,[26,27] implemented on Olex2.[28] All atoms except hydrogen were refined anisotropically. Hydrogen atoms were set in calculated positions and refined as riding atoms. Powder X-ray diffraction (PXRD) patterns of all compounds were obtained in a Bruker D8 Advance diffractometer (Bruker AXS, Karlsruhe, Germany) using Co Kα radiation. The samples were scanned from 2θ = 5-60°, with a step size of 0.05° and a counting time of 1 s *per* step. The phase purity of all samples was verified by comparison between PXRD diffractograms and those simulated from single-crystal data.

Magnetic measurements were carried out using a PPMS Quantum-Design DynaCool (Quantum Design, San Diego, California, USA) equipped with a 9 T magnet. Direct current magnetic data were recorded in the temperature range of 2-250 K for compound **2**, and 2-300 K for the others under applied DC magnetic field (H_{dc}) of 0.1 T. Field-dependent magnetization curves were measured at different temperatures (2 to 8 K) with a maximum magnetic field of 9 T. Dynamic magnetic properties of compounds **4** and **5** were studied by temperature and frequency-dependent AC magnetic susceptibility measurements in the range of 2.5-7 K and 10 Hz-10 kHz, under H_{dc} = 0 and H_{dc} = 0.2 T.

Syntheses

Compounds **1-6** were obtained through a one-pot strategy, as follows: 1.0 mmol of the lanthanide(III) nitrate (Ln^{3+} = Sm (**1**), Eu (**2**), Gd (**3**), Tb (**4**), Dy (**5**) and Er (**6**)) was added to 20 mL of an ethanolic solution containing 1.0 mmol of 4-picolinic acid. The colorless solution was heated to 60 °C and stirred for 3 h. Then, the resulting solution was slowly cooled to room temperature and kept undisturbed for slow solvent evaporation. Colorless single crystals of compounds **1-6** were filtered off after 15 days and washed with a small amount of cold ethanol. Infrared spectra of compounds **1-6** are shown in Figures S13-S18 (SI section).

$[Sm(NO_3)(4picH)_2(H_2O)_4](NO_3)_2$ (**1**)

Yield: 40.9%; IR (ATR) ν / cm^{-1} 3483, 3140-3078, 1582, 1402, 1582-1437, 1402, 1295, 1028, 862, 818, 766, 543, 417; anal. calcd. for $SmC_{12}H_{18}N_5O_{17}$: C 22.02, H 2.77, N 10.70%, found: C 21.97, H 2.67, N 10.55%.

$[Eu(NO_3)(4picH)_2(H_2O)_4](NO_3)_2$ (**2**)

Yield: 37.6%; IR (ATR) ν / cm^{-1} 3499, 3150-3077, 1582, 1402, 1582-1437, 1402, 1295, 1029, 862, 818, 766, 543, 418; anal. calcd. for $EuC_{12}H_{18}N_5O_{17}$: C 21.96, H 2.76, N 10.67%, found: C 22.04, H 2.89, N 10.70%.

$[Gd(NO_3)(4picH)_2(H_2O)_4](NO_3)_2$ (**3**)

Yield: 32.3%; IR (ATR) ν / cm^{-1} 3497, 3145-3078, 1581, 1404, 1581-1437, 1402, 1296, 1029, 862, 818, 766, 537, 417; anal. calcd. for $GdC_{12}H_{18}N_5O_{17}$: C 21.79, H 2.74, N 10.59%, found: C 21.92, H 2.63, N 10.42%.

$[Tb(NO_3)(4picH)_2(H_2O)_4](NO_3)_2$ (**4**)

Yield: 38.5%; IR (ATR) ν / cm^{-1} 3499, 3150-3078, 1581, 1404, 1581-1437, 1404, 1296, 1029, 861, 818, 766, 538, 417; anal. calcd. for $TbC_{12}H_{18}N_5O_{17}$: C 21.73, H 2.74, N 10.56%, found: C 21.56, H 2.61, N 10.28%.

$[Dy(NO_3)(4picH)_2(H_2O)_4](NO_3)_2$ (**5**)

Yield: 33.9%; IR (ATR) ν / cm^{-1} 3506, 3150-3077, 1582, 1404, 1582-1437, 1404, 1298, 1029, 861, 818, 767, 539, 418; anal. calcd. for $DyC_{12}H_{18}N_5O_{17}$: C 21.61, H 2.72, N 10.50%, found: C 21.96, H 2.64, N 10.34%.

$[Er(NO_3)(4picH)_2(H_2O)_4](NO_3)_2$ (**6**)

Yield: 38.7%; IR (ATR) ν / cm^{-1} 3499, 3151-3080, 1581, 1404, 1581-1437, 1404, 1298, 1029, 861, 818, 765, 539, 421; anal. calcd. for $ErC_{12}H_{18}N_5O_{17}$: C 21.46, H 2.70, N 10.43%, found: C 21.86, H 2.58, N 10.21%.

Computational details

All calculations were performed using the ORCA 5.0.3 software.[29] The geometries were optimized and the vibrational frequencies were calculated for 4-picolinic acid at the PBE0/def2-TZVP level (a triple-zeta valence polarized basis-set).[30] Since negative or imaginary frequencies were not observed, the geometries were taken as global minima and used as a base for vertical-transition time-dependent density functional theory (TD-DFT) calculations at the same level, which were carried out with 100 states to allow the selection of the most representative ones. The calculated Khom-Sham orbitals were generated with the Chemcraft 1.8 software.[31] The evaluation of the molecular orbitals was done through a Mulliken population analysis employing the Multiwfn software.[32]

We investigated the electronic and magnetic properties of structure **5** by employing Unrestricted Corresponding Orbitals[33] as the initial orbital guess, in conjunction with the Complete Active Space Self-Consistent Field (CASSCF) method.[34] All calculations incorporated the Douglas-Kroll-Hess relativistic approximation[35] using the DKH-Def2-TZVP basis set for non-metallic atoms and the SARC2-DKH-QZVP basis set (a quadruple-zeta valence polarized basis-set) for dysprosium. To account for perturbational treatment, the *Quasi*-Degenerate N-Electron Valence State Perturbation Theory (QD-NEVPT2)[36] was applied with the Nakano formulation.[37]

Two distinct configurations were employed for the CASSCF calculations: CAS(9,7) for 21 sextets and SA-CAS(9,7) for 21 sextets, 40 quartets, and 50 doublets. Spin-orbit coupling (SOC) contributions to the Zero-Field Splitting (ZFS) were determined using the CASSCF+QD-NEVPT2 wavefunctions and the *quasi*-degenerate perturbation theory (QDPT).[38] Crystal field (CF) parameters were derived using the *Ab Initio* Ligand-Field Theory (AILFT) implemented by Neese[39] in the ORCA package.

Results and Discussion

Syntheses

Synthesis of compounds **1-6** explored the one-pot reaction between lanthanide nitrates and 4-picolinic acid. This strategy afforded a series of mononuclear lanthanide-based compounds. For the six compounds, adding one equivalent of $Ln(NO_3)_3 \cdot xH_2O$ over a heated ethanolic solution of 4-picolinic acid did not result in any visible change even after the end of the reaction time. All solutions were then slowly cooled to room temperature and kept at rest for about two weeks, which resulted in the formation of translucent colorless single-crystals suitable for X-ray diffraction.

Although the synthetic procedure applied an equimolar ratio between the lanthanide salts and 4-picolinic acid, compounds **1-6** exhibited a 1:2 molar ratio, with the ligand being coordinated to the lanthanide ion in a monodentate fashion. Compounds **2** and **6** were previously described using the same molar ratio.[40,41] Furthermore, similar syntheses reported in the literature using gadolinium or ytterbium nitrates and the pyridine-3-carboxylic acid in a 1:2 ratio, but in basic conditions, afforded binuclear species with comparable yields obtained for **1-6**.[42] In all cases, it was not observed coordination through the pyridine nitrogen atom, and the pyridine-3-carboxylate acted as bridging ligand, connecting both lanthanide ions. Therefore, using an equimolar ratio and acid conditions seems to prevent additional coordination of carboxylate groups, affording mononuclear species only.

With respect to compounds **2** and **6** already reported, as the synthetic approaches were different from the one used in this work and no other properties were previously described, a full characterization of both compounds is discussed below.

Description of the crystal structures

Compounds **1-6** crystallized in a *C*2/c monoclinic space group, and their molecular structures consisted of mononuclear complexes, with the molecular formula $[Ln(NO_3)(4picH)_2(H_2O)_4](NO_3)_2$, in which Ln^{3+} stands for Sm (**1**), Eu (**2**), Gd (**3**), Tb (**4**), Dy (**5**) and Er (**6**). A generic representation of the isomorphic structure of compounds **1-6** can be seen in Figure 1a, while the crystallographic data and refinement parameters of **1-6** are gathered in Table S1 (SI section). Selected bond lengths and angles are shown in Table 1. Thermal ellipsoids are shown in Figures S19-S24 (SI section).

A careful inspection of the crystal structure revealed that the 4picH ligands consisted of neutral species, given their zwitterionic nature. The deprotonation of the carboxylic group was suggested by C1–O1 and C1–O2 bond lengths around 1.25 Å, which is an intermediate value between those of C=O and C–OH bond distances in the crystal structure of the 4-picolinic acid.[43] Therefore, to keep its neutrality, the pyridinic nitrogen atom must be necessarily protonated, making clear that complexes **1-6** are cationic species and assume a 2+ formal charge, which is balanced by the two nitrate anions in the crystal lattice.

The lanthanide ions in **1-6** are octa-coordinated to two 4picH oxygen atoms from two distinct moieties, one chelate nitrate anion, and four water oxygen atoms, exhibiting a

Table 1. Selected bond lengths for compounds **1-6**

Atom label	Compound **1** (Sm)	Compound **2** (Eu)	Compound **3** (Gd)	Compound **4** (Tb)	Compound **5** (Dy)	Compound **6** (Er)
Ln1–O1 / Å	2.3707(12)	2.3618(11)	2.3546(13)	2.344(3)	2.326(4)	2.311(2)
Ln1–O3 / Å	2.5122(14)	2.5004(14)	2.4892(16)	2.481(3)	2.466(5)	2.445(2)
Ln1–O5 / Å	2.3959(14)	2.3682(13)	2.3676(13)	2.362(2)	2.321(4)	2.298(2)
Ln1–O6 / Å	2.3804(14)	2.3820(13)	2.3522(12)	2.337(3)	2.335(4)	2.317(2)
C1–O1 / Å	1.254(2)	1.2539(19)	1.251(2)	1.250(4)	1.251(7)	1.245(3)
C1–O2 / Å	1.247(2)	1.245(2)	1.249(2)	1.250(5)	1.246(7)	1.254(4)

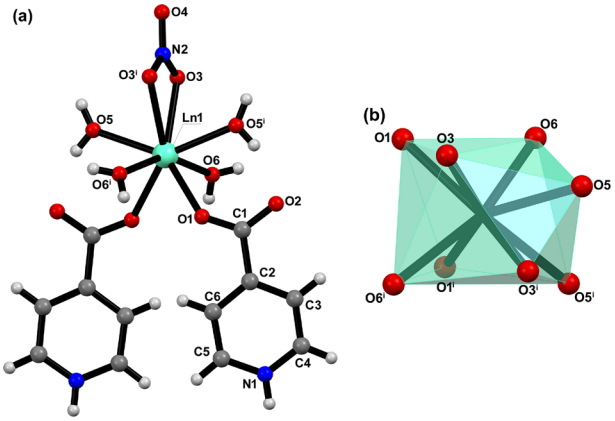

Figure 1. (a) Generic representation of the crystal structure of mononuclear compounds **1-6** with atom labels. Symmetry operation to generate equivalent atoms: (*i*) 1 – x, y, ½ – z. (b) Polyhedra around the lanthanide ion showing the coordination environment for the europium derivative.

distorted square antiprismatic geometry. This coordination environment is related to a D_{4d} local symmetry around lanthanide ions, as evaluated by SHAPE 2.1 software[44] (see Table S2 (SI section) for a list of the continuous shape measures for compounds **1-6**), which can be better visualized when the antiprism superior and inferior planes are formed by the atoms O1, O3, O5, and O6, and O1', O3', O5', and O6', respectively (Figure 1b). The 4picH ligand coordinates to the metal ion in a monodentate fashion by the O1 atom, with the Ln–$O_{(4picH)}$ bond lengths decreasing from 2.371(1) to 2.311(2) Å as the lanthanide ionic radius decreases in the row from samarium(III) to erbium(III) (see Table 1). With respect to the bidentate nitrate ligand, the same tendency was found in the Ln–O3 bond lengths, which are slightly longer than those found for the 4picH ligands and range from 2.5122(14) to 2.445(2) Å. Such Ln–$O_{(4picH)}$ and Ln–O3 values are typical for lanthanide complexes containing carboxylate and nitrate ligands reported elsewhere.[45]

The crystal lattice in all compounds is stabilized by a network of intra- and intermolecular hydrogen bonds that follow a common pattern. Selected geometric parameters associated with these interactions can be found in Tables S3-S8 (SI section). A fragment of the crystal packing for compound **1** is shown in Figure 2a as a representative example of the series. The free carboxylate oxygen atom takes part in both intramolecular hydrogen bonds involving one of the coordinated water molecules (O6, violet dashed lines) and an intermolecular hydrogen bond between the carboxylic moiety and a neighboring water molecule (O5, green dashed lines). The latter promotes the formation of a 1D supramolecular array along the *c*-axis, as seen in Figure 2a. Within this supramolecular chain, the shortest distance between lanthanide ions is ca. 7.3 Å. In addition, each aqua ligand interacts with the NO_3^- counterions, giving rise to an $O_{(nitrate)}\cdots H–O_{(Water)}$ hydrogen bond network, as detailed in Figure 2b (orange dashed lines). Finally, the crystal packing of compounds **1-6** is further stabilized by intermolecular interaction between the protonated pyridinic nitrogen atom (N1) and the nitrate oxygen atoms (light green dashed lines in Figure 2b), generating a double supramolecular chain running along the *b* axis with a lanthanide separation of ca. 12 Å.

The phase purity of compounds **1-6** was confirmed by comparing the experimental X-ray powder diffraction

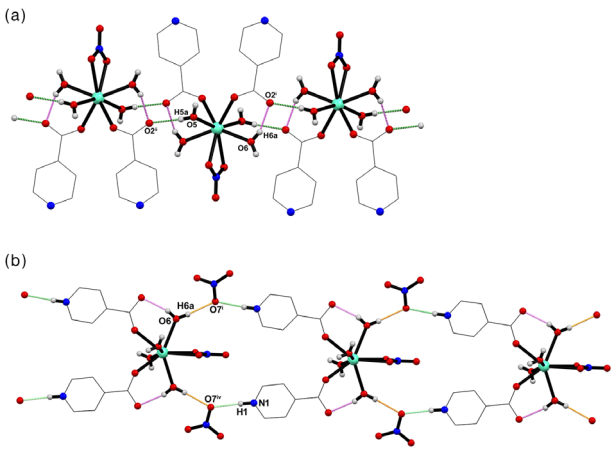

Figure 2. Details of the crystal packing of compound **1** showing the supramolecular chains running along the *c* (a) and *b* axes (b). Some hydrogen atoms were omitted, and carbon atoms are represented as wires for clarity. Symmetry operations to generate equivalent atoms: (*i*) –x + 1, y, –z + 3/2; (*ii*) –x + 1/2, –y + 1/2, –z + 1; (*iv*) x, y + 1, z.

patterns and the simulated ones obtained by single-crystal X-ray diffraction (SC-XRD), as depicted in Figures S25-S30 (SI section).

Absorption spectroscopy and theoretical calculations

Solid-state UV-Vis experimental absorption spectra of compounds **1-6** are presented in Figures S31-S36 (SI section). Two strong absorption bands appear in all of them, around 6.20 eV (200 nm) and between 4.73-4.40 eV (262-282 nm), and also occur in the spectrum of 4-picolinic acid, at 5.30 and 4.79 eV (234 and 270 nm, respectively). Thus, these strong bands can be attributed to π-π* transitions centered on the 4picH ligand. In order to support the experimental data, TD-DFT calculations of vertical electronic excitation energies were performed for the 4-picolinic acid (Figure 3) at the PBE0/def2-TZVP level, based on the optimized geometry obtained from the same method (Figure S37, SI section), whose results are presented in Figure 3 and Table 2.

The theoretical results also showed two main transitions, at 241.8 and 199.5 nm (5.13 and 6.21 eV, respectively), allowing the attribution of the experimental ones. The assignment of those transitions as π→π* was based on a Mulliken population analysis performed on the frontier calculated molecular orbitals (Table 3). Besides, the density of states analysis developed from the Mulliken population (Figure 4) exhibited a higher contribution of the pyridine moiety to the majority of orbitals, both occupied and unoccupied, indicating that, in general, the electronic transitions are centered on Py orbitals.

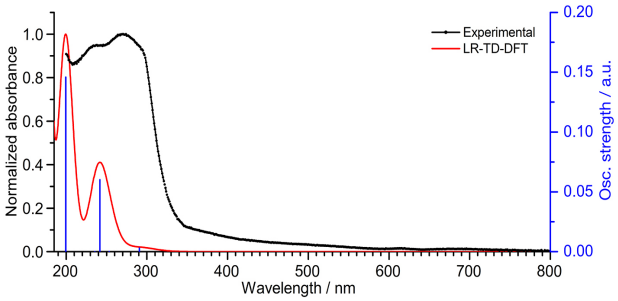

Figure 3. Experimental and theoretical UV-Vis absorption spectra of 4-picolinic acid.

The sharp absorption bands observed in the solid-state absorption spectra of compounds **1**, **2**, **5**, and **6** were assigned as f-f transitions (Table 4) as stated by a comprehensive work concerning lanthanide(III) free-ion spectra elaborated by Carnall *et al.*[46,47] This choice is justified by the fact that the f orbitals in lanthanides are weakly affected by the coordination environment, and thus the absorption bands would not display great energy displacements in the complexes studied compared to those ions in water.[48]

Table 2. Selected linear response vertical excitation energies and oscillator strengths calculated for 4-picolinic acid. Isosurface: 0.03

No.[a]	λ[b] (energy / eV) / nm	*f*[c] / au	One-electron excitation components[d]		Assignment[e] / %		Experimental
			h^+	e^-			λ_{max}[f] (energy / eV) / nm
3	241.8 (5.13)	0.0601	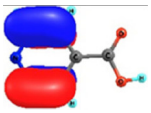 HOMO-1	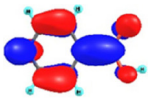 LUMO	π→π*	82.9	270 (4.59)
			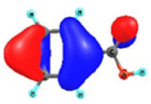 HOMO-3	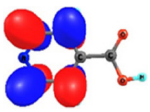 LUMO+1	π→π*	14.9	
5	199.5 (6.21)	0.1460	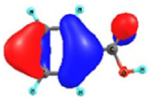 HOMO-3	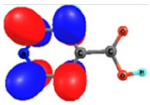 LUMO+1	π→π*	73.8	234 (5.30)
			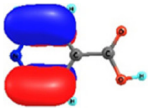 HOMO-1	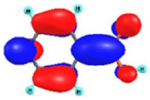 LUMO	π→π*	19.9	

[a]Number of the calculated transition; [b]calculated wavelength; [c]oscillator strength; [d]major contribution from one-electron excitations to the transition, represented as a hole-particle excitation ($h^+ \rightarrow e^-$); [e]the assignments were done based on Mulliken population analysis; [f]experimental wavelength.

Table 3. Energy and Mulliken population analysis for the frontier orbitals of 4-picolinic acid

Orbital	Energy / eV	Mulliken population
L+1	−0.75	π^*Py (99.7% of Py)
L	−2.02	π^*Py + π^*COOH (70.3% of Py; 29.7% of COOH)
H	−7.75	πPy + πCOOH (97.1% of Py; 2.9% of COOH)
H-1	−7.97	πPy (99.4% of Py)
H-2	−8.60	πPy + πCOOH (14.8% of Py; 85.2% of COOH)
H-3	−8.71	πPy + πCOOH (85.4% of Py; 14.6% of COOH)

Py: pyridine ring; COOH: carboxylic acid moiety.

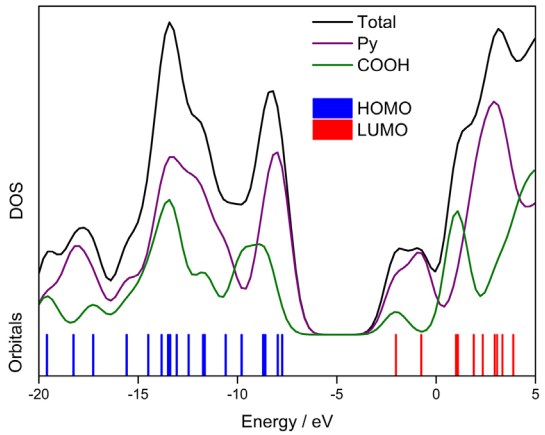

Figure 4. Energy level diagram of 4-picolinic acid calculated at PBE0/def2-TZVP and density of states (DOS) analysis.

Table 4. Assignments of the f-f transitions observed in the solid-state UV-Vis spectra of compounds **1**, **2**, **5**, and **6**

Compound	λ_{max}[a] / nm	λ_{exp}[b] (free ion) / nm	λ_{calc}[c] (free ion) / nm	Assignment[d]
1	363	361	361	$^6H_{5/2} \rightarrow {}^4D_{3/2}$
	376	–	376	$^6H_{5/2} \rightarrow {}^4D_{1/2}$
	416	416	415	$^6H_{5/2} \rightarrow {}^6P_{5/2} + {}^4P_{5/2}$
	402	–	404	$^6H_{5/2} \rightarrow {}^4F_{7/2}$
2	395	394	394	$^7F_0 \rightarrow {}^5L_6$
	465	465	465	$^7F_0 \rightarrow {}^5D_2$
5	352	350	350	$^6H_{15/2} \rightarrow {}^6P_{7/2}$
	365	365	364	$^6H_{15/2} \rightarrow {}^6P_{5/2}$
	389	388	389	$^6H_{15/2} \rightarrow {}^4F_{7/2}$
	452	452	449	$^6H_{15/2} \rightarrow {}^4I_{15/2}$
	761	755	757	$^6H_{15/2} \rightarrow {}^6F_{3/2}$
6	375	359	359	$^4I_{15/2} \rightarrow {}^2G_{7/2}$
	365	366	366	$^4I_{15/2} \rightarrow {}^4G_{9/2}$
	379	379	379	$^4I_{15/2} \rightarrow {}^4G_{11/2}$
	406	409	410	$^4I_{15/2} \rightarrow {}^2G_{9/2} + {}^4F_{9/2}$
	443	445	447	$^4I_{15/2} \rightarrow {}^4F_{3/2}$
	450	451	454	$^4I_{15/2} \rightarrow {}^4F_{5/2}$
	488	488	490	$^4I_{15/2} \rightarrow {}^4F_{7/2}$
	521	526	524	$^4I_{15/2} \rightarrow {}^2H_{11/2} + {}^4G_{11/2}$
	543	546	542	$^4I_{15/2} \rightarrow {}^4S_{3/2}$
	654	659	658	$^4I_{15/2} \rightarrow {}^4F_{9/2}$

[a]Experimental wavelength; [b]experimental wavelength of the free ions in water obtained from the publications Carnall *et al.*;[46,47] [c]calculated wavelength of the free ions in water obtained from the publications Carnall *et al.*;[46,47] [d]obtained from the publications Carnall *et al.*[46,47]

Emission spectroscopy

Solid-state emission spectra of compounds **1-6** were obtained from macerated single-crystal samples excited at 280 nm. This specific wavelength was used due to the higher absorption observed for all complexes in this spectral region, which was attributed to the 4picH intraligand π→π* transition. Likewise, the excitation spectra were obtained by applying a wavelength corresponding to that of the higher intensity emission of each compound. Compounds **1**, **2**, **4**, and **5** displayed an emissive profile with sharp and intense bands in the visible region due to the f-f transitions. These emission bands result from a ligand energy transfer to the excited states of lanthanide ions, the so-called antenna effect.[49] This emission profile was not seen for the gadolinium- and erbium-derivatives (compounds **3** and **6**). Excitation spectra are shown in Figures S38-S41 (SI section).

Concerning the emission spectrum of **2** (Figure 5), five bands predominantly located in the red region arose from the radiative decays of the excited state $^5D_0$ to levels ^7F_J (J = 0, 1, 2, 3, 4), which were assigned as follows: $^5D_0 \rightarrow {}^7F_0$ (579 nm), $^5D_0 \rightarrow {}^7F_1$ (593 nm) $^5D_0 \rightarrow {}^7F_2$ (614 nm), $^5D_0 \rightarrow {}^7F_3$ (650 nm), $^5D_0 \rightarrow {}^7F_4$ (700 nm). The higher intensity of the $^5D_0 \rightarrow {}^7F_2$ transition with respect to the $^5D_0 \rightarrow {}^7F_1$ indicates that the forced electric dipole and the dynamic coupling mechanisms are predominant in relation to magnetic dipole one.[50] The two intense emission bands at 614 and 700 nm are known as environment-sensible transitions and indicate the ability of a europium-based compound to behave as a luminescent probe.[51] The $^5D_0 \rightarrow {}^7F_2$ transition follows the selection rule ΔJ = 2 and is classified as a hypersensitive one, meaning that its intensity is more affected by changes in the chemical environment. The strongest intensity of the band at 614 nm in comparison to the others suggests that the europium(III) ion lies in a non-centrosymmetric environment in **2**, given its parity-forbidden nature.[52] The forbidden $^5D_0 \rightarrow {}^7F_0$ transition features the lowest intensity in the spectrum due to the D_{4d} symmetry found for the europium(III) ion in the crystal structure. However, its

presence could also be attributed to an apparent reduction of the local symmetry when **2** is irradiated due to the mixing of wavefunctions of different terms caused by crystal field perturbations.[53,54]

The Judd-Ofelt theory was applied to evaluate the emission intensities of the $^5D_0 \rightarrow {}^7F_J$ (J = 2, 4) levels of europium(III) of **2**. The Ω_2 and Ω_4 intensity parameters were calculated using JOES 4.0 software[21] and are listed in Table 5. The Ω_2 parameter is environmental-dependent and affected by the covalence between the lanthanide ion and ligands, while Ω_4 is related to the long-range effects.[55,56] The comparison between both parameters revealed $\Omega_2 < \Omega_4$ in the solid state, indicating a high symmetry around the metal ion and a higher ionic character involving europium(III) and 4picH ligand.[55]

The CIE 1931 (Commission Internationale de I'Eclairage) chromaticity diagram[57] was generated from the respective emission spectrum, and the value of color coordinates (x, y) was found to be x = 0.63434 and y = 0.33509 (inset, Figure 5). These coordinates values confirm the emission in the orange-red region and suggest compound **2** as a possible red component in a tricolor based organic light-emitting diodes (OLEDs).[58]

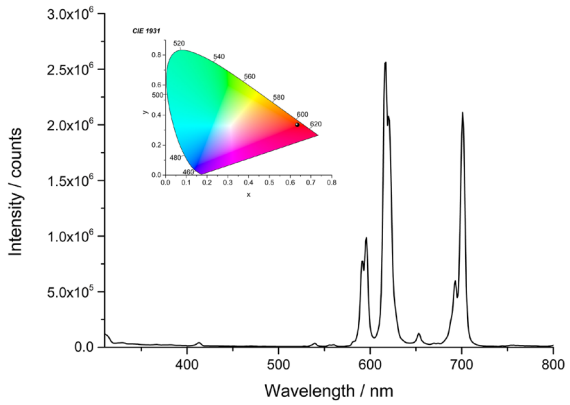

Figure 5. Solid state emission spectrum for compound **2**. Excitation wavelength: 280 nm. Inset: chromaticity diagram (CIE 1931) showing the emission color (coordinates: x = 0.63434 and y = 0.33509).

The luminescence of compound **2** was also studied in frozen glassy solution (EtOH/MeOH, 4:1) at 77 K and in ethanolic solution at 298 K (Figure S42, SI section). The emissive profiles at 77 and 298 K are like those obtained from the solid state sample with the same five transitions observed. Emission bands associated with $^5D_0 \rightarrow {}^7F_2$ and $^5D_0 \rightarrow {}^7F_4$ in solid state display changes in their intensities compared to the spectrum obtained in solution or frozen solution. Moreover, it is important to highlight that in the spectrum recorded in solution at 298 K (Figure S42b), the intensity of the $^5D_0 \rightarrow {}^7F_0$ decay is relatively higher than that observed in the solid sample, reinforcing the observation of local symmetry reduction. Such variations reflect in the integrated area of the bands and, consequently, change the Judd-Ofelt parameter values (see Table 5 for details). Given the sensibility of $^5D_0 \rightarrow {}^7F_2$ and $^5D_0 \rightarrow {}^7F_4$ transitions, a change in the emission profile of emission bands can be associated with variations in the coordination environment. At 77 K $\Omega_2 < \Omega_4$, while at 298 K an inversion was found for calculated Judd-Ofelt parameters, with Ω_2 slightly higher than Ω_4. This trend revealed a decrease in the symmetry around the europium(III) ion and an increase in the covalency of the Eu–O bonds when the complex is in solution at 298 K.[55,59] It is important to highlight that recent works[60,61] pointed to a temperature dependence of Ω_4, in which it increases as the temperature decreases, as well seen in the data listed in Table 5 for compound **2**.

The luminescence lifetimes of the radiative emission $^5D_0 \rightarrow {}^7F_2$ at 614 nm of compound **2** were evaluated from both the solid sample and the ethanolic solution. The fit of photoluminescence decay curves using the equation $I_{(t)} = I_{(0)} \exp(-t/\tau)$, where τ, I_0, and I stand for decay time, and the luminescence intensities at time 0 s and t, respectively, afforded luminescence lifetimes of 180 μs (solid), 326 μs (solution at 298 K), and 340 μs (solution at 77 K). The obtained values fall in the typical range found for other europium-based compounds.[50,58] The total decay rates in solid and solution, A_{total}, were derived from the reciprocal of lifetime values ($A_{total} = 1/\tau$), while the radiative rates were obtained by JOES 4.0 software[21] by summation of individual radiative rates from $^5D_0 \rightarrow {}^7F_1$ and $^5D_0 \rightarrow {}^7F_{2,4}$ transitions. Compound **2** exhibits radiative and non-radiative decay rates (A_{rad} and A_{nrad}) of 285 and 5210 s^{-1} in solid, 216 and 2852 s^{-1} in solution at 298 K, and 228 and 2731 s^{-1} in frozen glass solution at 77 K (Table 5). The higher value of A_{nrad} reflects a luminescence-quenching because of O–H vibrations from the four water molecules in the first coordination sphere.[62] The quantum efficiency (η) was calculated from equation 1, affording values of 5.2 (solid), 7.0 (solution at 298 K) and 7.8% (solution at 77 K). As a result of the lowest non-radiative decay rate in solution, a slightly higher η value was observed and might be caused by the replacement of some water by ethanol molecules, which reduces the number of O–H bonds around the metal ion, and, consequently, the energy loss from vibration.

$$\eta = A_{rad}/(A_{rad} + A_{nrad}) \quad (1)$$

The spectrum of the terbium-based compound shows seven bands that arose from the $^5D_4$ excited state radiative decay to ^7F_J levels, where J = 0-6 (Figure 6). The green emission displayed after excitation results from the intense

Table 5. Photoluminescence parameters for compound **2**

	Ω_2 / 10^{-20} cm^{-2}	Ω_4 / 10^{-20} cm^{-2}	τ / μs	A_{total} / s	A_{rad} / s	A_{nrad} / s	η / %
Solid	5.095	6.856	182	5495	285	5210	5.2
Solution 298 K	6.456	5.975	326	3068	216	2852	7.0
Solution 77 K	4.345	11.603	338	2959	228	2731	7.7

Ω_2: Judd-Ofelt parameter for the $^5D_0 \rightarrow {}^7F_2$ transition; Ω_4: Judd-Ofelt parameter for the $^5D_0 \rightarrow {}^7F_4$ transition. τ: decay time; A_{total}: total decay rate; A_{rad}: radiative decay rate; A_{nrad}: non-radiative decay rate; η: quantum efficiency.

band at 547 nm, assigned as the $^5D_4 \rightarrow {}^7F_5$ transition. Other bands were seen at 492 ($^5D_4 \rightarrow {}^7F_6$), 584 and 593 ($^5D_4 \rightarrow {}^7F_4$), 622 ($^5D_4 \rightarrow {}^7F_3$), 649 and 655 ($^5D_4 \rightarrow {}^7F_2$), 671 ($^5D_4 \rightarrow {}^7F_1$) and 681 nm ($^5D_4 \rightarrow {}^7F_0$). The presence of the strong band at 547 nm associated with the environment-sensible nature of $^5D_4 \rightarrow {}^7F_{6,4,2}$ decays support compound **4** as a candidate for a luminescent probe. The green emission in the solid state was also evaluated using the CIE 1931 chromaticity diagram,[57] and the color coordinates (x, y) were found to be x = 0.343 and y = 0.574 (inset, Figure 6).

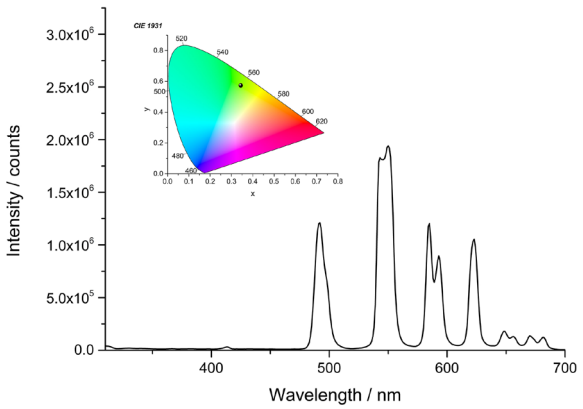

Figure 6. Solid state emission spectrum for compound **4**. Excitation wavelength: 280 nm. Inset: chromaticity diagram (CIE 1931) showing the emission color (coordinates: x = 0.343 and y = 0.574).

Similarly, to the europium complex, the emission of compound **4** in solution displays a profile close to the observed one in the solid state. It is important to stress that at 77 K (Figure S43a, SI section), the intensity of the bands is higher than those seen at 298 K (Figure S43b, SI section), which suggests a luminescence quenching process at 298 K caused by the higher vibrational state of molecules at room temperature.[63] The energy loss through the non-radiative path is such that low-intensities bands associated with $^5D_4 \rightarrow {}^7F_0$ and $^5D_4 \rightarrow {}^7F_1$ decays are absent in the spectrum obtained at 298 K; nevertheless, once the $^5D_4 \rightarrow {}^7F_5$ band remains present at both temperatures, compound **4** can still be seen as a possible candidate for luminescent probe in solution. The luminescence lifetimes of the radiative emission $^5D_4 \rightarrow {}^7F_5$ at 545 nm in solid, solution at 298 and 77 K are 605, 983 and 1074 μs, respectively.

Unlike Eu^{3+} and Tb^{3+}-based compounds, complexes **1** and **5** displayed emission bands in the ultraviolet region when excited at 280 nm in the solid state (Figures 7 and 8). These same bands are also seen in the emission spectrum of the 4-picolinic acid, indicating that transitions observed in the spectra of compounds **1** and **5** originate from this moiety. Together with UV emissions, bands in the visible region can be seen in the spectrum of compounds **1** and **5**, which were assigned as *f-f* transitions.

The visible portion of the spectrum in compound **1** exhibits four bands associated with Sm^{3+} characteristic emissions. Decays from excited state $^4G_{5/2}$ to levels ^6H_J (J = 5/2, 7/2, 9/2, 11/2) were attributed to such bands. The higher energy emission is found at 565 nm, and its corresponding transition $^4G_{5/2} \rightarrow {}^6H_{5/2}$ occurs through an electric-dipole (ED) mechanism. The most intense emission was found at 598 nm and was assigned to the $^4G_{5/2} \rightarrow {}^6H_{7/2}$ transition, mediated by a magnetic dipole mechanism. Other emission bands can be found at 645 and 705 nm, associated with $^4G_{5/2} \rightarrow {}^6H_{9/2}$ and $^4G_{5/2} \rightarrow {}^6H_{11/2}$ transitions, respectively. Similar to previously discussed analogs, the existence of high-intensity ED bands attests to a lower local symmetry of Sm^{3+} ion in this complex. The radiative decays afford a pinkish emission in the solid state, which was also evaluated by using the CIE 1931 chromaticity diagram resulting in color coordinates (x, y) of 0.370 and 0.276 (inset, Figure 7). The luminescence lifetimes of the

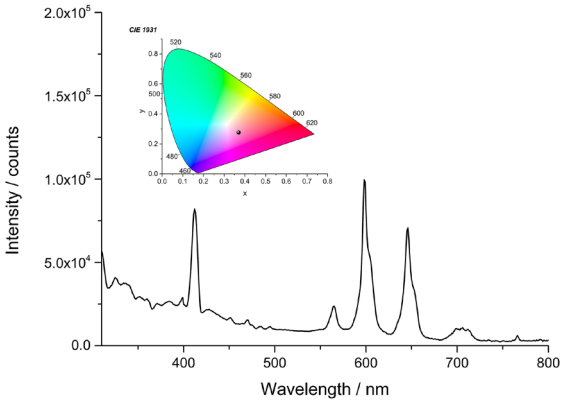

Figure 7. Solid state emission spectrum for compound **1**. Excitation wavelength: 280 nm. Inset: chromaticity diagram (CIE 1931) showing the emission color (coordinates: x = 0.370 and y = 0.276).

radiative emission at 598 nm in solid, solution at 298 and 77 K are 5, 0.490 and 3.23 μs, respectively.

For compound **5**, four emission bands attributed to the decay of the excited state $^7F_{9/2}$ to levels ^6H_J, in which J = 15/2, 13/2, 11/2, and 9/2, were observed. The emission at higher energy was found at 482 and 488 nm due to the MD $^7F_{9/2} \rightarrow {}^6H_{15/2}$ decay. The most intense emission band was found in the yellow region of the spectrum (578 nm), and it is classified as environmentally sensitive and arises from the $^7F_{9/2} \rightarrow {}^6H_{13/2}$ decay. As this transition happens through an electric dipole, it is correct to assume that the Dy^{3+} lies in a low local symmetry in complex **5**, given the intensity of the band. Furthermore, two weak bands are observed at 662 and 752 nm and are characterized as $^7F_{9/2} \rightarrow {}^6H_{11/2}$ and $^7F_{9/2} \rightarrow {}^6H_{9/2}$ transitions, respectively. The luminescence lifetimes of the radiative emission at 576 nm in solid, solution at 298 and 77 K are 4.4 μs, 9.0 μs and 5.5 μs, respectively.

Accordingly to the CIE 1931 coordinates obtained from the chromaticity diagram, the white emission of compound **5** (x = 0.313 and y = 0.319) is very close to the pure white (x = 0.33 and y = 0.33). Based on these coordinates and McCamy's approximation (equations 2 and 3),[64,65] the correlated color temperature (CCT) for compound **5** was estimated at 6570 K, which lies in the typical values found for commercial white light-emitting diodes (LED) devices.

$$CCT = -437n^3 + 3601n^2 - 6861n + 5514.31 \quad (2)$$

$$n = (x - 0.3320)/(y - 0.1858) \quad (3)$$

where x and y are the CIE 1931 coordinates.

The white emission arose from the combination of emission bands from the 4picH ligand and the lanthanide when irradiated at 280 nm. This kind of emission is usually obtained through a dichromatic combination between yellow and blue emitting sources, which is in concordance with the emission profile displayed by compound **5**.[20] In addition to its function as a sensitizer ligand in compound **5**, the 4picH moiety plays an important role in balancing the yellow emission centered on lanthanide ion. This combination provided a rare candidate for single-ion white-light emitters (the color rendering index (CRI) is another parameter used to fully classify a compound as a white-light emitter, but its evaluation is out-of-scope of this work).

Some radiative decays attributed to the 4picH ligand below 450 nm (Figures 7 and 8) indicated a possible loss of the efficiency of the zwitterionic moiety as a sensitizer in compounds **1** and **5** in comparison to that observed in Eu^{3+} and Tb^{3+} derivatives. Such conclusions corroborate the data extracted from excitation spectra of compounds **2** and **4**, where the bands associated with ligands found at 263 and 316 nm are more intense than those deriving from metal centers; this suggests a greater efficiency in the intramolecular energy transfer when compared to compounds **1** and **5**. In addition, excitation spectra of compounds **1** and **5** display the ligand excitation bands of the same or even lower intensity than metal ones. Such behavior can be justified by a higher energy gap between the energy levels of the ligand triplet excited state ($^3\pi$, π^*) and the metal emissive state ([Ln^{3+}]*).

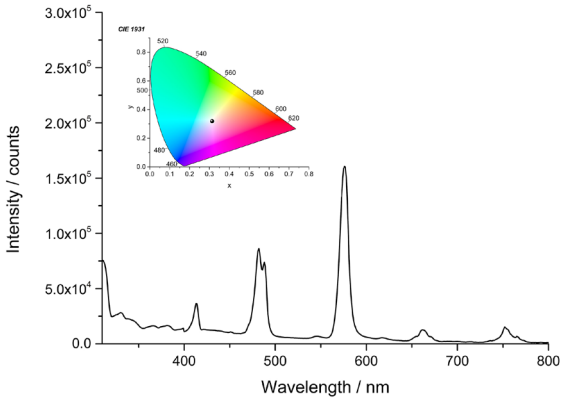

Figure 8. Solid state emission spectrum for compound **5**. Excitation wavelength: 280 nm. Inset: chromaticity diagram showing the emission color (coordinates: x = 0.313 and y = 0.319).

The evaluation of 4picH triplet and singlet states energies was carried out using the emission spectra recorded at 77 and 298 K for the gadolinium-based compound (Figure S44, SI section). The energy transfer from ligand to the lanthanide ion occurs in four steps, namely: (*i*) absorption of the UV light to the singlet state of 4picH moieties at 35,714 cm^{-1}; (*ii*) intersystem-crossing from the excited singlet state to the triplet state at 27,100 cm^{-1} and (*iii*) energy transfer from ligand to the lanthanide, and finally (*iv*) luminescence emission.

The triplet and singlet energies of 4-pic are consistent with a similar ligand published elsewhere.[66] The triplet energy was taken from the shortest wavelength of phosphorescence obtained at 77 K, the lifetime of 2.87 μs for Gd^{3+} complex at 77 K is consistent with a phosphorescence process from the ligand.

Table 6 lists the observed λ_{max} of emission bands in each compound's spectrum and the transitions to which they were assigned.

Magnetic properties

The magnetic properties have been investigated in the 2-300 K temperature range for compounds **1**, **3-6** and 2-250 K for compound **2**. The temperature dependence of the $\chi_M T$ product, where χ_M is the molar magnetic

Table 6. Emission assignments for compounds **1**, **2**, **4**, and **5** in solid state and solution

Compound	Sample (temperature / K)	λ_{max}[a] and assignments / nm
1	solid (298)	$^4G_{5/2}\rightarrow{}^6H_J$: 565 (J = 5/2); 598 (J = 7/2); 645 (J = 9/2), 705 (J = 11/2)
2	solid (298)	$^5D_0\rightarrow{}^7F_J$: 579 (J = 0), 589, 593 (J = 1) 614, 618, 620 (J = 2); 650,651 (J = 3); 686, 690, 691, 697, 700. 702 (J = 4)
	solution (77)	329-460 ($\pi^*\rightarrow\pi$); $^5D_0\rightarrow{}^7F_J$: 580 (J = 0); 592 (J = 1); 615, 618 (J = 2); 649 (J = 3); 686, 695 (J = 4)
	solution (298)	327, 399 ($\pi^*\rightarrow\pi$); $^5D_0\rightarrow{}^7F_J$: 579 (J = 0); 591 (J = 1); 618 (J = 2); 649 (J = 3); 686, 693, 696 (J = 4)
4	solid (298)	$^5D_4\rightarrow{}^7F_J$: 492 (J = 6); 547 (J = 5); 584,593 (J = 4); 622 (J = 3); 649,655 (J = 2); 671 (J = 1); 681 (J = 0)
	solution (77)	329 ($\pi^*\rightarrow\pi$); $^5D_4\rightarrow{}^7F_J$: 489 (J = 6); 541, 544 (J = 5); 584 (J = 4); 621 (J = 3); 646, 649 (J = 2); 667 (J = 1); 678 (J = 0)
	solution (298)	318 ($\pi^*\rightarrow\pi$); $^5D_4\rightarrow{}^7F_J$: 489 (J = 6); 542, 544 (J = 5); 584, 589 (J = 4); 621 (J = 3); 650 (J = 2)
5	solid (298)	$^4F_{9/2}\rightarrow{}^6H_J$: 482, 488 (J = 15/2); 578 (J = 13/2); 622 (J = 11/2); 752 (J = 9/2)

[a]Emission wavelength.

susceptibility, is shown in Figure 9 for all compounds. The $\chi_M T$ values at room temperature are 0.4 (**1**), 7.8 (**3**), 11.4 (**4**), 14.5 (**5**), and 11.2 (**6**) $cm^3\ mol^{-1}\ K$ and 0.9 $cm^3\ mol^{-1}\ K$ for **2** at 250 K. For compounds **3-6**, these values are close to the expected ones for non-interacting Ln^{3+} free ions (7.9, 11.8, 14.2 and 11.5 $cm^3\ mol^{-1}\ K$, respectively).[67] On the other hand, for compounds **1-2**, due to thermally populated excited states at room temperature, the $\chi_M T$ values are quite different from the free ion ones, as expected.[67]

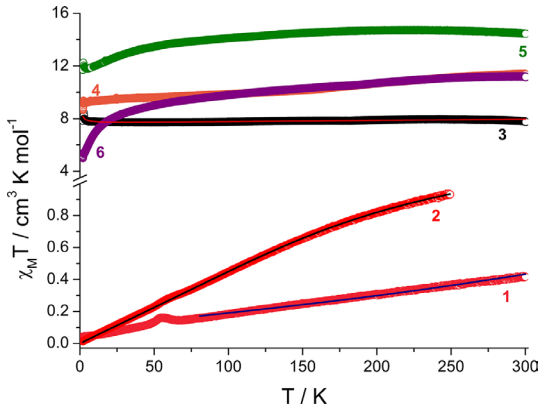

Figure 9. Thermal dependences of the $\chi_M T$ product for compounds **1-6** under static field H = 0.1 T. Solid red and black lines represent the best fits (see text and SI section for details).

As discussed in the crystal structure descriptions, the intermolecular distances between the lanthanide ions along the chains and between neighboring chains are large. Therefore, all intermolecular magnetic interactions are expected to be very weak. Since Gd^{3+} has an $^8S_{7/2}$ ground term with no magnetic anisotropy, the $\chi_M T$ variations of compound **3** would reflect the magnetic interactions between the spin carriers. For compound **3**, by decreasing the temperature, $\chi_M T$ remains almost constant down to 6 K, then increases slightly, showing the occurrence of weak intermolecular ferromagnetic couplings and/or dipolar interactions. A simple mean-field approximation was used to estimate the interaction (see SI section). The parameters obtained from the fit are g = 1.97 for the Landé g-factor and zJ' = 0.01 cm^{-1}, with z the number of neighbors and J' the intermolecular coupling constant, corresponding to very weak ferromagnetic interactions. Looking back at the crystal structure, the molecular units are linked through hydrogen bonds between the coordinated water and the free oxygen of 4picH. These hydrogen bonds can provide a path to the ferromagnetic interaction through the spin polarization mechanism (Figure S45, SI section). Isothermal magnetization was also measured at low temperatures, and the superposition of the curves in the plot M *vs*. H/T (magnetization *versus* magnetic field over temperature) reflects the magnetic isotropic character of the Gd^{3+} ion (Figures S46, SI section).

For compounds **1**-**2** and **4-6**, as the temperature is lowered, the $\chi_M T$ values decrease continuously. Since the analysis of the crystal structure and the magnetic response of compound **3** indicate that there is almost no magnetic interaction between the lanthanide ions in these compounds, their magnetic behavior results mostly from the individual contribution of the metal ions. With respect to compounds **1** and **2**, the ground term of the lanthanide ion (^6H and ^7F) is split by the spin-orbit interaction into six and seven states, respectively. The depopulation of the low-lying spin-orbit coupled states is therefore responsible for the decrease of $\chi_M T$.[67,68] The magnetic data were successfully analyzed considering only the spin-orbit coupling of the lanthanide ions (see SI section for the equations), and the best fits are shown in Figure 9 with λ = 310 and 390 cm^{-1}, respectively, which are consistent with the literature.[68-70] The peak observed between 45 and 70 K for compound **1** is due to slight oxygen contamination in the sample chamber. Therefore, the fit was performed from 80 K to room temperature.

On the contrary, for compounds **4-6**, the magnetic behavior comes from the depopulation of the crystal-field

split states (Stark sublevels). The task of modelling the magnetic response of compounds containing lanthanide ions other than Gd^{3+} is very complex, generally involving many parameters, which is beyond the scope of this study. Field-dependent magnetization was measured at low temperatures for compounds **4-6** (Figures S47, SI section). The curves are very similar, with a sharp increase at low fields and a linear one for larger fields without saturation. At 2 K and 7 T, the magnetic moment reaches a value of 7.6, 6.4, and 6.1 $N\mu_B$ (N stands for the Avogadro number, and μ_B is the Bohr magneton) for compounds **4-6**, respectively, which are significantly lower than the theoretical ones (9, 10 and 9 $N\mu_B$ respectively), suggesting the presence of magnetic anisotropy and/or low-lying excited states. Finally, the non-superposition of the reduced magnetization curves confirms the presence of magnetic anisotropy for these compounds (Figures S48, SI section).

The dynamic magnetic properties of compounds **4** and **5** were investigated by frequency and temperature-dependent AC magnetic susceptibility measurements. Under zero static magnetic field, the in-phase and out-of-phase components show no frequency dependence for both compounds (Figures S49-S52, SI section), which could result from quantum tunnelling of the magnetization (QTM) that may be particularly fast for single-ion magnets (SIMs). It is well-known that the QTM process can be hampered when a non-zero static magnetic field is applied. Therefore, the AC measurements were also performed under a static magnetic field of 0.2 T. For compound **4**, no clear frequency dependence of the AC susceptibility was observed (Figures S53-S54, SI section). In contrast, compound **5** exhibited strong frequency-dependent in-phase and out-of-phase components of the magnetic susceptibility (Figures S55 and 10, SI section), confirming the slow relaxation of the magnetization at low temperatures. To extract the relaxation times and to obtain the Arrhenius plot (Figures S56, SI section),

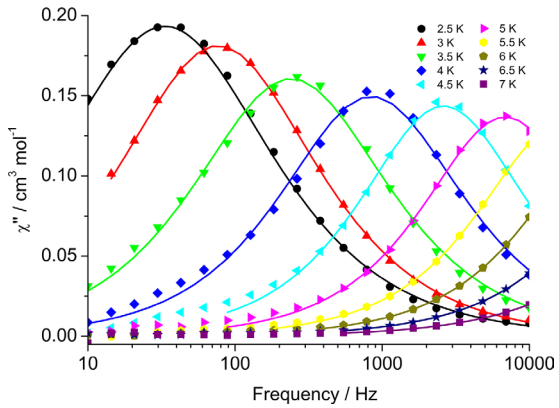

Figure 10. Isothermal frequency dependence of the out-of-phase AC magnetic susceptibility for compound **5** (H_{dc} = 0.2 T).

the in-phase and out-of-phase data were fitted with the same generalized Debye model.[71,72] In the Arrhenius plot, the observed temperature dependence of the relaxation times is not a straight line, showing the occurrence of other relaxation processes than the Orbach one. Several attempts considering different processes (direct, Orbach, Raman, QTM) were unsuccessful, usually resulting in non-physical parameters. Therefore, only the Orbach process was used to fit the relaxation times for the highest temperatures (see Figure S56 in SI section). The best fit results gave an effective energy barrier $\Delta E/k_B = 43 \pm 2$ K and a pre-exponential factor $\tau_0 = (4.0 \pm 1.6) \times 10^{-9}$ s which are consistent with other Dy^{3+} mononuclear with SIM behavior.[73-75]

CASSCF calculations

The CASSCF calculations demonstrated that a highly multiconfigurational nature characterizes the ground state in compound **5**. It is primarily composed of a 56.2% $f_0^{(1)}$, $f_{+1}^{(2)}$, $f_{-1}^{(2)}$, $f_{+2}^{(1)}$, $f_{-2}^{(1)}$, $f_{+3}^{(1)}$, $f_{-3}^{(1)}$ configuration, and 34.4% $f_0^{(1)}$, $f_{+1}^{(1)}$, $f_{-1}^{(1)}$, $f_{+2}^{(2)}$, $f_{-2}^{(2)}$, $f_{+3}^{(1)}$, $f_{-3}^{(1)}$. In addition, several other configurations contribute to the ground state, albeit with less than 2% significance. Comparing the state-averaged (SA-CASSCF) and single-state CASSCF calculations revealed that the sextet multiplicity is the most relevant. The first quartet state appears at approximately 25,000 cm^{-1} above the sextet ground state, while the first doublet state is found at around 37,000 cm^{-1}. Results from both CASSCF and state-averaged calculations are nearly identical, which further corroborates that the sextet state is the most significant. As expected, the *f* orbitals manifest in a *quasi*-degenerate configuration with relative energy splits of 0.0, 1.8, 79.3, 119.6, 223.2, 441.3, and 505.9 cm^{-1}.

The calculated spin-orbit coupling constant (ξ) for molecule **5** is 1936.37 cm^{-1}, which deviates only by approximately 28 cm^{-1} from the expected free-ion value.[76] The ground $^6H_{15/2}$ term appears with a Kramers multiplet that consists of a mixture of the effective |±3/2> and |±1/2> spins. Additionally, the anisotropic z and y axes point towards the coordination waters, as illustrated in Figure 11. The qualitative effective energy barrier predicted for the first Zeeman eigenstate is 77.96 K, which is in close agreement with the experimental measurement.

Conclusions

A series of mononuclear lanthanide-based compounds was obtained by a mild synthetic strategy and characterized by several techniques. One of the main findings of this work

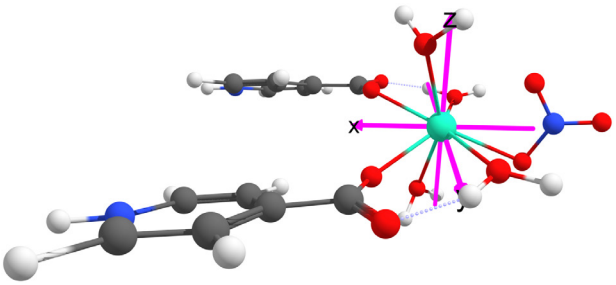

Figure 11. *Ab initio* anisotropic axis x, y, and z aligned with respect to the molecular frame of compound **5**.

is the description of the zwitterionic form of the 4-picolinic acid as an antenna ligand. This property afforded intense emission processes for compounds **1**, **2**, **4**, and **5** when excited by a wavelength of 280 nm. Based on these results, the europium and terbium derivatives can be assigned as potential probes in solution since they kept the emission under such conditions. Moreover, the combination between blue emission of the zwitterionic form of 4-picolinic acid and that from the dysprosium ion in **5** leads to white-light emission, making this compound a candidate for application in lightning devices, electronic displays, and as mercury-based fluorescent material substitutes. Finally, the interesting combination between white-light emitting and single-ion magnet behavior in compound **5** opens possibilities for new multifunctional materials.

Supplementary Information

Crystallographic data for the structures in this work were deposited in the Cambridge Crystallographic Data Centre as supplementary publication numbers CCDC 2251501-22501506. Copies of the data can be obtained, free of charge, via https://www.ccdc.cam.ac.uk/structures/.

Supplementary data (SC-XRD, PXRD, theoretical calculations, UV-Vis and excitation spectra) are available free of charge at http://jbcs.sbq.org.br as a PDF file.

Acknowledgments

The authors thank the financial support from Fundação Carlos Chagas de Amparo à Pesquisa do Estado do Rio de Janeiro-FAPERJ (project numbers E-26/202.720/2018, E-26/010.000978/2019 and E-26/201.314/2022), Conselho Nacional de Desenvolvimento Científico e Tecnológico-CNPq (project numbers 423086/2018-9 and 304671/2020-7). This work was also supported by Coordenação de Aperfeiçoamento de Pessoal de Nível Superior-Brasil (CAPES), within the Capes-PrInt program, financial code 001, project number 88887.310269/2018-00. E.S.A. and A.C.C.N. acknowledge CAPES for funding their fellowship. B.P.R. thanks FAPERJ for the Master Nota 10 scholarship. We are grateful to LDRX-UFF, LAME-UFF and CBPF for the use of laboratory facilities. Theoretical calculations were performed using the Lobo Carneiro supercomputer from Núcleo Avançado de Computação de Alto Desemprenho (NACAD), under the Project ID a20006 and the Sagarana Cluster from CEPAD-Centro de Processamento de Alto Desempenho ICB/UFMG. The authors would also like to thank the National Laboratory for Scientific Computing (LNCC/MCTI, Brazil) for providing HPC resources of the SDumont supercomputer, which have contributed to the research results reported within this paper.

Author Contributions

Esther S. Areas was responsible for conceptualization, data curation, formal analysis, investigation, methodology, validation, visualization, writing original draft and writing-review and editing; Bruno P. Rodrigues for conceptualization, data curation, formal analysis, investigation, methodology, validation, visualization, writing original draft, review and editing; Ana Carolina C. do Nascimento for conceptualization, data curation, formal analysis, investigation, methodology, validation, visualization, writing original draft, review and editing; Henrique C. S. Junior for conceptualization, data curation, formal analysis, investigation, methodology, validation, visualization, writing original draft, review and editing; Glaucio B. Ferreira for conceptualization, data curation, formal analysis, funding acquisition, investigation, methodology, project administration, resources, supervision, validation visualization, writing original draft, review and editing; Fabio S. Miranda for conceptualization, data curation, formal analysis, investigation, methodology, supervision, validation, visualization and writing-review and editing; Flávio Garcia for conceptualization, data curation, formal analysis, investigation, methodology, visualization and writing review and editing; Syed H. Safeer for data curation, formal analysis, investigation, methodology, visualization; Stéphane Soriano for conceptualization, data curation, formal analysis, investigation, methodology, validation, visualization, writing original draft, review and editing; Guilherme P. Guedes for conceptualization, data curation, formal analysis, funding acquisition, investigation, methodology, project administration, resources, supervision, validation, visualization, writing original draft.

References

1. Aykanat, A.; Meng, Z.; Benedetto, G.; Mirica, K. A.; *Chem. Mater.* **2020**, *32*, 5372. [Crossref]
2. Coronado, E.; *Nat. Rev. Mater.* **2020**, *5*, 87. [Crossref]
3. Zhao, L.; Zhang, W.; Qiong, W.; Fu, C.; Ren, X.; Ly, K.; Ma, T.; Chen, X.; Tan, L.; Meng, X.; *J. Nanobiotechnol.* **2022**, *20*, 133. [Crossref]

4. Fueyo-González, F.; Garcia-Fernandez, E.; Martínez, D.; Infantes, L.; Orte, A.; González-Vera, J. A.; Herranz, R.; *Chem. Commun.* **2020**, *56*, 5484. [Crossref]
5. Magott, M.; Brzozowska, M.; Baran, S.; Vieru, V.; Pinkowicz, D.; *Nat. Commun.* **2022**, *13*, 2014. [Crossref]
6. Huang, Y.; Zhao, Y.; Liu, Y.; Xu, B.; Xu, S.; Bai, G.; *Mater. Des.* **2021**, *210*, 110023. [Crossref]
7. Anwar, Z. M.; Ibrahim, I. A.; Kamel, R. M.; Abdel-Salam, E. T.; El-Asfoury, M. H.; *J. Mol. Struct.* **2018**, *1154*, 272. [Crossref]
8. Miroshnichenko, A. S.; Deriabin, K. V.; Baranov, A. I.; Neplokh, V.; Mitin, M. D.; Kolesnikov, I. E.; Dobrynin, M. V.; Parshina, E. K.; Mukhin, I. S.; Islamova, R. M.; *ACS Appl. Polym. Mater.* **2022**, *4*, 2683. [Crossref]
9. Ishikawa, N.; Sugita, M.; Ishikawa, T.; Koshihara, S.-y.; Kaizu, Y.; *J. Am. Chem. Soc.* **2003**, *125*, 8694. [Crossref]
10. Parker, D.; Fradgleya, J. D.; Wong, K.-L.; *Chem. Soc. Rev.* **2021**, *50*, 8193. [Crossref]
11. Chen, Z.; Ho, C.-L.; Wang, L.; Wong, W.-Y.; *Adv. Mater.* **2020**, *32*, 1903269. [Crossref]
12. Chen, Y.; Sun, L.; Chang, S.; Chen, L.; Zhao, J.; *Inorg. Chem.* **2018**, *57*, 15079. [Crossref]
13. Chen, W.-T.; Wen, J.-W.; Luo, Z.-G.; Yao, Z.-L.; *Synth. React. Inorg., Met.-Org., Nano-Met. Chem.* **2013**, *44*, 1464. [Crossref]
14. Feng, X.; Chen, J.-L.; Wang, L.-Y.; Xie, S.-Y.; Yang, S.; Huo, S.-Z.; Ng, S.-W.; *CrystEngComm* **2014**, *16*, 1334. [Crossref]
15. Lis, S.; Piskula, Z.; Kubicki, M.; *Mater. Chem. Phys.* **2009**, *114*, 134. [Crossref]
16. Leng, X.; Hao, W.; Yang, X.; Zhang, Z.; Li, H.; Ma, Y.; Cheng, Y.; Schipper, D.; *Inorg. Chem.* **2022**, *61*, 8484. [Crossref]
17. Wang, X.; Liu, Y.; Jin, M.; Wu, Y.; Chen, L.; Zhao, J.-W.; *Cryst. Growth Des.* **2017**, *17*, 5295. [Crossref]
18. Garcia, G. F.; Guettas, D.; Montigaud, V.; Larini, P.; Sessoli, R.; Totti, F.; Cador, O.; Pilet, G.; Le Guennic, B.; *Angew. Chem.* **2018**, *130*, 17335. [Crossref]
19. Yang, Q.-Y.; Wu, K.; Jiang, J.-J.; Hsu, C.-W.; Pan, M.; Lehn, J.-M.; Su, C.-Y.; *Chem. Commun.* **2014**, *50*, 7702. [Crossref]
20. Lekshmi, S. S.; Remya, A. R.; Reddy, M. L. P.; Varughese, S.; *J. Photochem. Photobiol., C* **2017**, *33*, 109. [Crossref]
21. Ćirić, A.; Stoiadinović, S.; Sekulić, M.; Dramićanin, M. D.; *J. Lumin.* **2019**, *205*, 351. [Crossref]
22. *OriginPro*, 9.1; OriginLab Corporation, Northamptom, Massachusetts, USA, 2013.
23. *APEX3*, V2017.3-0; Bruker AXS Inc., USA, 2018.
24. *SAINT*, V8.38A; Bruker AXS Inc., USA, 2017.
25. Sheldrick, G. M.; *SADABS*, V2.03; University of Göttingen, Germany, 2002.
26. Sheldrick, G. M.; *Acta Crystallogr., Sect. A: Found. Crystallogr.* **2008**, *64*, 112. [Crossref]
27. Sheldrick, G. M.; *Acta Crystallogr., Sect. C: Struct. Chem.* **2015**, *71*, 3. [Crossref]
28. Dolomanov, O. V.; Bourhis, L. J.; Gildea, R. J.; Howard, J. A. K.; Puschmann, H.; *J. Appl. Cryst.* **2009**, *42*, 339. [Crossref]
29. Neese, F.; *Wiley Interdiscip. Rev.: Comput. Mol. Sci.* **2022**, *12*, e1606. [Crossref]
30. Adamo, C.; Barone, V.; *J. Chem. Phys.* **1999**, *13*, 6158. [Crossref]
31. Chemcraft, version 1.8, build 648, https://www.chemcraftprog.com, accessed in September 2023.
32. Tian, L.; Feiwu, C.; *J. Comput. Chem.* **2012**, *33*, 580. [Crossref]
33. King, H. F.; Stanton, R. E.; Kim, H.; Wyatt, R. E.; Parr, R. G.; *J. Chem. Phys.* **1967**, *47*, 1936. [Crossref]
34. Roos, B. O.; Taylor, P. R.; Siegbahn, P. E. M.; Sigbahn, P. E. M.; Siegbahn, P. E. M.; *Chem. Phys.* **1980**, *48*, 157. [Crossref]
35. Nakajima, T.; Hirao, K.; *Chem. Rev.* **2012**, *112*, 385. [Crossref]
36. Angeli, C.; Cimiraglia, R.; Evangelisti, S.; Leininger, T.; Malrieu, J. P.; *J. Chem. Phys.* **2001**, *114*, 10252. [Crossref]
37. Nakano, H.; *J. Chem. Phys.* **1993**, *99*, 7983. [Crossref]
38. Nakano, H.; Uchiyama, R.; Hirao, K.; *J. Comput. Chem.* **2002**, *23*, 1166. [Crossref]
39. Mingos, D. M. P.; Day, P.; Dahl, J. P.; Atanasov, M.; *Molecular Electronic Structures of Transition Metal Complexes II*; Springer Berlin: Heidelberg, Germany, 2012.
40. Zhong, Z.-G.; Song, J.-F.; Li, J.; Meng, Z.-H.; *Acta Crystallogr. E: Crystallogr. Commun.* **2011**, *E67*, m637. [Crossref]
41. Chen, W.-T.; Luo, Q.-Y.; Liu, D.-S.; Chen, H.-L.; Xu, Y.-P.; *Inorg. Chem. Commun.* **2008**, *11*, 899. [Crossref]
42. Hojnik, N.; Kristl, M.; Golobic, A.; Jaglicic, Z.; Drofenik, M.; *Cent. Eur. J. Chem.* **2014**, *12*, 220. [Crossref]
43. Takusagawa, F.; Shimada, A.; *Chem. Lett.* **1973**, *2*, 1089. [Crossref]
44. Llunell, M.; Casanova, D. J.; Alemany, P.; Alvarez, S.; *SHAPE*, 2.1; Universitat de Barcelona, Spain, 2013.
45. Chen, X.-Y.; Goff, G. S.; Ewing, W. C.; Scott, B. L.; Runde, W.; *Inorg. Chem.* **2012**, *24*, 13254. [Crossref]
46. Carnall, W. T.; Fields, P. R.; Rajnak, K.; *J. Chem. Phys.* **1968**, *49*, 4424. [Crossref]
47. Carnall, W. T.; Fields, P. R.; Rajnak, K.; *J. Chem. Phys.* **1968**, *49*, 4450. [Crossref]
48. Singh, A. K.; *Coord. Chem. Rev.* **2022**, *455*, 214365. [Crossref]
49. Junker, A. K. R.; Hill, L. R.; Thompson, A. L.; Faulkner, S.; Sørensen, T. J.; *Dalton Trans.* **2018**, *47*, 4794. [Crossref]
50. Queiroz, E. C.; Franco, C. H. J.; Ferreira, M. S.; Freire, R. O.; Machado, F. C.; *J. Lumin.* **2022**, *249*, 118990. [Crossref]
51. Han, L.-J.; Kong, Y.-J.; Hou, G.-Z.; Chen, H.-C.; Zhang, X.-M.; Zheng, H.-G.; *Inorg. Chem.* **2020**, *59*, 7181. [Crossref]
52. Cotton, S.; *Lanthanide and Actinide Chemistry*, 1st ed.; John Wiley & Sons: Rutland, UK, 2006.
53. Bettencourt-Dias, A.; *Luminescence of Lanthanide Ions in Coordination Compounds and Nanomaterials*, 1st ed.; John Wiley & Sons: West Sussex, UK, 2014.

54. Wolfbeis, O. S.; *Lanthanide Luminescence: Photophysical, Analytical and Biological Aspects*; Springer-Verlag: Berlin, Germany, 2011.
55. Ferhi, M.; Bouzidi, C.; Horchani-Naifer, K.; Elhouichet, H.; Ferid, M.; *Opt. Mater.* **2014**, *37*, 607. [Crossref]
56. Kumar, M.; Seshagiri, T. K.; Godbole, S. V.; *Phys. B: Condens. Matter* **2013**, *410*, 141. [Crossref]
57. Smith, T.; Guild, J.; *Trans. Opt. Soc.* **1931**, *33*, 73. [Crossref]
58. Devi, R.; Dala, M.; Bala, M.; Khatkar, S. P.; Taxak, V. B.; Boora, P.; *J. Mater. Sci.: Mater. Electron*. **2016**, *27*, 12506. [Crossref]
59. Binnemans, K.; *Coord. Chem. Rev.* **2015**, *295*, 1. [Crossref]
60. Ćirić, A.; Stojadinović, S.; Dramićanin, M. D.; *Phys. B: Condens. Matter*. **2020**, *579*, 411891. [Crossref]
61. Manh, N.C.; Nguyen, L. T. H.; Xuan, T. M.; Tra, H. D.; Duong, T. T. A.; Nguyen, L. T. T.; Pham, H. V.; Ha, M. N.; Nguyen, V. H.; Chau, H. D.; Tran, T. K. N.; *J. Lumin.* **2023**, *258*, 119776. [Crossref]
62. Resende Filho, J. B. M.; Silva, J. C.; Vale, J. A.; Brito, H. F.; Faustino, W. M.; Espínola, J. G. P.; Felinto, M. C. F. C.; Teotonio, E. E. S.; *J. Braz. Chem. Soc.* **2014**, *25*, 2080. [Crossref]
63. Valeur, B.; *Molecular Fluorescence: Principle and Applications*, 1st ed.; Wiley-VCH: New York, USA, 2001.
64. McCamy, C. S.; *Color Res. Appl.* **1992**, *17*, 142. [Crossref]
65. Li, C.; Cui, G.; Melgosa, M.; Ruan, X.; Zhang, Y.; Ma, L.; Xiao, K.; Luo, M. R.; *Opt. Express* **2016**, *24*, 14066. [Crossref]
66. Godlewska, P.; Hanuza, J.; Hermanowicz, K.; Lisiecki, R.; Lorenc, J.; Ryba-Romanowski, W.; Kucharska, E.; Ptak, M.; Macalik, L.; *Opt. Mater.* **2020**, *109*, 110208. [Crossref]
67. Kahn, O.; *Molecular Magnetism*; VCH Publishers Inc.: New York, USA, 1993.
68. Andruh, M.; Bakalbassis, E.; Kahn, O.; Trombe, J. C.; Porchers, P.; *Inorg. Chem.* **1993**, *32*, 1616. [Crossref]
69. Kido, T.; Ikuta, Y.; Sunatsuki, Y.; Ogawa, Y.; Matsumoto, N.; *Inorg. Chem.* **2003**, *42*, 398. [Crossref]
70. Escobar, L. B. L.; Guedes, P. G.; Soriano, S.; Cassaro, R. A. A.; Marbey, J.; Hill, S.; Novak, M. A.; Andruh, M.; Vaz, M. G. F.; *Inorg. Chem.* **2018**, *57*, 326. [Crossref]
71. Cole, K. S.; Cole, R. H.; *J. Chem. Phys.* **1941**, *9*, 341. [Crossref]
72. Costes, M.; Broto, J. M.; Raquet, B.; Rakoto, H.; Novak, M. A.; Sinnecker, J. P.; Soriano, S.; Folly, W. S. D.; Maignan, A.; Hardy, V. J.; *J. Magn. Magn. Mater.* **2005**, *294*, e123. [Crossref]
73. Vaz, R. C. A.; Esteves, I. O.; Oliveira, W. X. C.; Honorato, J.; Martins, F. T.; Marques, L. F.; Santos, G. L.; Freire, R. O.; Jesus, L. T.; Pedroso, E. F.; Nunes, W. C.; Julye, M.; Pereira, C. L. M.; *Dalton Trans.* **2020**, *49*, 16106. [Crossref]
74. Ali, B.; Li, X.-L.; Gendron, B. L.; Guennic, B. L.; Tang, J.; *Dalton Trans.* **2021**, *50*, 5146. [Crossref]
75. Wang, R.; Yao, B.; Bai, F.; Wang, W.; Li, L.; Ma, Y.; Wang, O.; Zhao, B.; Zhang, Y.; *Cryst. Eng. Comm.* **2021**, *23*, 1718. [Crossref]
76. Bronova, A.; Bredow, T.; Glaum, R.; Riley, M. J.; Urland, W.; *J. Comput. Chem.* **2018**, *39*, 176. [Crossref]

Submitted: April 26, 2023
Published online: September 27, 2023